Mon. Not. R. Astron. Soc. **000**, 1–12 (2009) Printed 27 January 2009 (MN LATEX style file v2.2)

Properties of the ionized gas in HH 202. I: Results from integral field spectroscopy with PMAS⋆

A. Mesa-Delgado[1]†, L. López-Martín[1], C. Esteban[1], J. García-Rojas[2], and V. Luridiana[3]
[1] *Instituto de Astrofísica de Canarias, E-38200 La Laguna, Tenerife, Spain*
[2] *Instituto de Astronomía, UNAM, Apdo. Postal 70-264, 04510 México D.F., Mexico*
[3] *Instituto de Astrofísica de Andalucía (CSIC), Apdo. Correos 3004, E-18080 Granada, Spain*

Accepted 2008 December 12. Received 2008 December 10; in original form 2008 October 24

ABSTRACT
We present results from integral field spectroscopy with the Potsdam Multi-Aperture Spectrograph of the head of the Herbig-Haro object HH 202 with a spatial sampling of $1''\times1''$. We have obtained maps of different emission lines, physical conditions –such as electron temperature and density– and ionic abundances from recombination and collisionally excited lines. We present the first map of the Balmer temperature and of the temperature fluctuation parameter, t^2. We have calculated the t^2 in the plane of the sky, which is substantially smaller than that determined along the line of sight. We have mapped the abundance discrepancy factor of O^{2+}, ADF(O^{2+}), finding its maximum value at the HH 202-S position. We have explored the relations between the ADF(O^{2+}) and the electron density, the Balmer and [O III] temperatures, the ionization degree as well as the t^2 parameter. We do not find clear correlations between these properties and the results seem to support that the ADF and t^2 are independent phenomena. We have found a weak negative correlation between the O^{2+} abundance determined from recombination lines and the temperature, which is the expected behaviour in an ionized nebula, hence it seems that there is not evidence for the presence of super-metal rich droplets in H II regions.

Key words: ISM: abundances – Herbig-Haro objects – ISM: individual: Orion Nebula – ISM: individual: HH 202

1 INTRODUCTION

The Orion Nebula is the nearest, most observed and studied Galactic H II region. It is an active star-formation region where phenomena associated with the early stages of stellar evolution such as protoplanetary disks (proplyds) and Herbig-Haro (HH) objects can be observed in detail.
HH objects are bright nebulosities associated with high-velocity gas flows. The most prominent high-velocity feature in the nebula is the Becklin-Neugebauer/Kleinmann-Low (BN/KL) complex, which contains several HH objects (HH 201, 205, 206, 207 and 208). But also, there are other important high-velocity flows that do not belong to the BN/KL complex, as is the case of HH 202, 203 and 204. The origin of these flows has been associated with infrared sources embedded within the Orion Molecular Cloud 1 South (see O'Dell & Henney 2008, and references therein).
HH 202 was one of the first HH objects identified in the Orion Nebula by Cantó et al. (1980) in their [S II] and [N II] images as an emission line object showing two bright knots –the so-called HH 202-N and HH 202-S (see Figure 1)– embedded in a more extended nebulosity with a long concave form. After its discovery, the spectroscopic work by Meaburn (1986) showed that the arc-shaped nebulosity emits in [O III] lines.
Further high-spectral resolution spectroscopy in several emission lines ([O I], [S II], [N II], [O II], [S III] and Hα) has been performed in HH 202 by O'Dell et al. (1991) who studied HH 202-S and found two velocity components. More recently, we can find in the literature extensive works on the gas kinematics in the Orion Nebula as those by Doi et al. (2002) and O'Dell & Doi (2003), where tangential velocities have been measured, or Doi et al. (2004), who provide with accurate radial velocity measurements, detecting up

⋆ Based on observations collected at the Centro Astronómico Hispano Alemán (CAHA) at Calar Alto, operated jointly by the Max-Planck Institut für Astronomie and the Instituto de Astrofísica de Andalucía (CSIC).
† E-mail: amd@iac.es

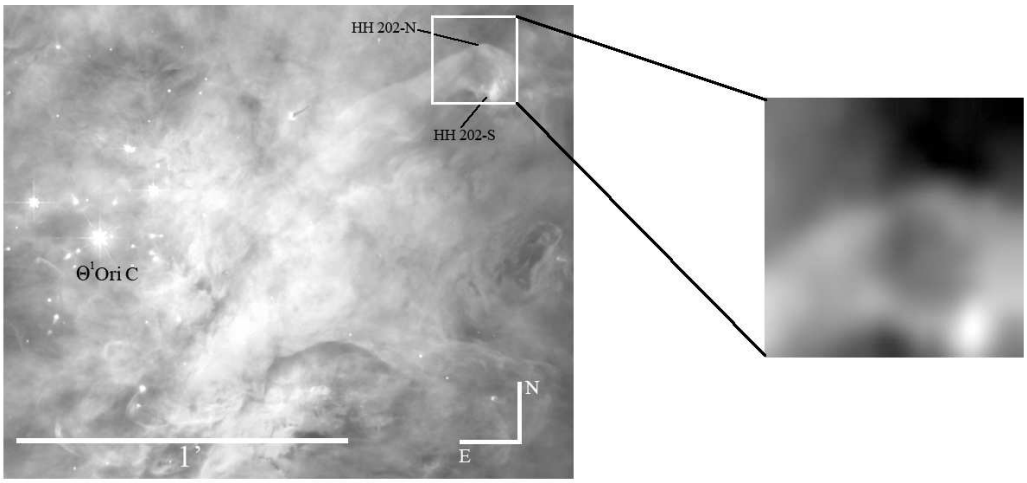

Figure 1. *HST* image of the central part of the Orion Nebula, which combines WFPC2 images taken in different filters (O'Dell & Wong 1996). The white square corresponds to the field of view of PMAS IFU used, covering the head of HH 202. The separate close-up image on the right shows the Hα map obtained with PMAS. The original map is 16×16 pixels of 1″×1″ size and has been rebinned to 160×160 pixels. Note the remarkable similarity between the *HST* image and our rebinned PMAS Hα map.

to three kinematic components in HH 202-S. On the other hand, the most detailed imaging study of the Orion Nebula in the [S II], [O III] and Hα lines has been carried out by O'Dell et al. (1997) with the Hubble Space Telescope (*HST*). These authors also detect an intense [O III] emission in the extended nebulosity of HH 202 and a strong [S II] emission at its knots. The extended [O III] emission found in all the works indicates that the main excitation mechanism of HH 202 is photoionization, most probably from the brightest and hottest star of the Trapezium cluster, θ^1 Ori C. This particular property –not very common in other HH objects, which are usually ionized by shocks– permits to derive the physical conditions and chemical abundances of the high velocity gas associated with HH 202 making use of the standard techniques for the study of ionized nebulae.

Our group has studied in detail the chemical composition of the Orion Nebula in some previous papers (Esteban et al. 1998, 2004; Mesa-Delgado et al. 2008) and is especially interested in studying the so-called abundance discrepancy (AD) problem in H II regions, which is the disagreement between the abundances of the same ion derived from collisionally excited lines (CELs) and recombination lines (RLs). From intermediate and high resolution spectroscopy of Galactic and extragalactic H II regions, our group has found that the O^{2+}/H^+ ratio calculated from RLs is always between 0.1 and 0.3 dex higher than the value obtained from CELs for the same region (see García-Rojas & Esteban 2007). The results obtained for H II regions are quite different to those obtained for planetary nebulae (PNe), where the AD shows a much wider range of values and could be substantially larger in some objects (*e.g.* Liu et al. 2000, 2006; Tsamis et al. 2003, 2004). As argued in García-Rojas & Esteban (2007), the AD problem in H II regions seems to be consistent with the predictions of the temperature fluctuaction paradigm proposed by Peimbert (1967) and parametrized by the mean square of the spatial distributions of temperature, the so-called t^2 parameter. In this scenario, the AD would be produced by the very different temperature dependence of the emissivities of both kinds of lines. In any case, the existence and origin of such temperature fluctuations are still controversial. Tsamis & Péquignot (2005) and Stasińska et al. (2007) have proposed a different hypothesis in order to explain the AD in H II regions. Based on the model for heavy-element mixing of Tenorio-Tagle (1996), the presence of cold metal-rich droplets of supernova ejecta still not mixed with the ambient gas of the H II regions would produce most of the RL emission while CEL emission would be produced by the ambient gas, wich would have the typical electron temperature of an H II region and the expected composition of the local interstellar medium. In such case, the abundances from CELs would be the truly representative ones of the nebula.

Several authors have studied the spatial distribution of the physical conditions in the Orion Nebula. O'Dell et al. (2003) have obtained a high-spatial resolution map of the electron temperature in a field centered at the southwest of the Trapezium cluster from narrowband images taken with the *HST*. They found small spatial scale temperature variations, which seem to be in quantitative agreement with the t^2 parameter determined using the AD factor found by Esteban et al. (2004). On the other hand, Rubin et al. (2003) have taken long-slit spectroscopy making use of *STIS* at the *HST* in several positions and do not find substantial spatial variations or gradients of the physical conditions along their slits positions. More recently, Sánchez et al. (2007) have obtained a mosaic of the Orion Nebula from integral field spectroscopy with a spatial resolution of 2.″7, but lacking a confident absolute flux calibration due to bad transparency during the observations. Their electron temperature map shows clear spatial variations and the electron density map is very rich in substructures, some of which could be related to HH objects. A more detailed view –but based on long-slit spectroscopy– has been obtained by Mesa-Delgado et al. (2008), who obtained spatial distributions –at spatial scales of 1.″2– of electron temperature, density, line intensities, ionic abundances and the AD factor (ADF, defined as the difference between the abundances derived from RLs and CELs) for five slit positions crossing different morphological zones of the Orion Nebula, finding spikes in the distribution

of the electron temperature and density which are related to the position of proplyds and HH objects. In particular, these authors found that the ADF shows larger values at the HH objects.

The use of the integral field spectroscopy is still in its infancy in the study of ionized nebulae and the number of works available is still rather small. In the case of PNe, Tsamis et al. (2008b) have carried out the first deep study using this technique with FLAMES at the VLT taking spectra of three PNe of the Galactic disc and covering the spectral range from 3964 to 5078 Å. For the Orion Nebula, Tsamis et al. (2008a) have presented preliminary results of integral field spectrocopy with FLAMES for several proplyds with the aim of studying the behaviour of the physical conditions, chemical abundances and the ADF in and outside these kinds of objects. The first results show that the temperature measured in the proplyds can be affected by collisional deexcitation as has been also suggested in previous works (Rubin et al. 2003; Mesa-Delgado et al. 2008).

The main goal of the present paper is to use integral field spectroscopy at spatial scales of 1" in order to explore the effect of HH objects on the derived ADF considering the results of Mesa-Delgado et al. (2008).

In §2 we describe the observations obtained with PMAS and the reduction procedure. In §3 we describe the emission line measurements and the reddening correction as well as some representative bidimensional maps of those quantities. In §4 we describe the determination of the physical conditions, chemical abundances –from both kinds of lines, CELs and RLs– and the ADF of O^{2+} as well as their corresponding maps. In §5 we calculate the t^2 parameter from different methods and present the first bidimensional map of this quantity. Also, we show the possible correlations among the ADF and the rest of properties determined. Finally, in §6 we summarize our main conclusions.

2 OBSERVATIONS AND DATA REDUCTION

HH 202 was observed on 2007 October 14 at Calar Alto Observatory (Almería, Spain), using the 3.5m Telescope with the Potsdam Multi-Aperture Spectrometer (PMAS, Roth et al. 2005). The standard lens array integral field unit (IFU) of $16''\times16''$ field of view (FOV) was used with a sampling of $1''$. Most of the optical range was covered with the V600 grating using two grating rotator angles: -72, covering from 3500 to 5100 Å; and -68, covering from 5700 to 7200 Å. The effective spectral resolution was 3.6 Å. The position of the IFU covering HH 202 is shown in Figure 1 where we can see the two bright knots HH 202-N and HH 202-S together with an Hα image obtained with PMAS rebinned to 160×160 pixels using the REBIN function of IDL which performs an expansion of the original map through a linear interpolation. The blue and red spectra have a total integration time of 1800 and 1000 seconds, respectively. Additional short exposures of 10 seconds were taken in order to avoid saturation of the brightest emission lines. Calibration images were obtained during the night: arc lamps for the wavelength calibration and a continuum lamp needed to extract the 256 individual spectra on the CCD. Observations of the spectrophotometric standard stars BD +28°4211, Feige 110 and G 191-B2B (Oke 1990) were used for flux calibration. The error of this calibration is of the order of 5%. The night was photometric and the typical seeing during the observations was $1''$.

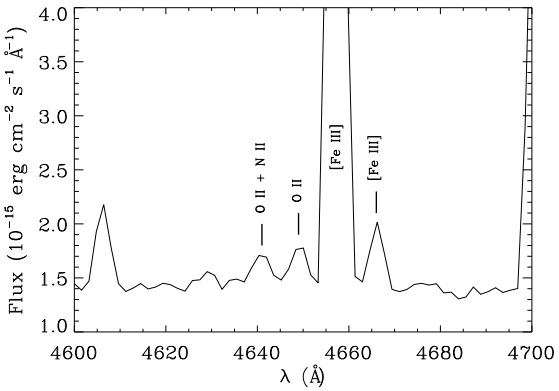

Figure 2. Section of a PMAS spectra around O II lines of multiplet 1 corresponding to the spaxel position (-5.5, -6.5).

The data were reduced using the IRAF reduction package SPECRED. After bias subtraction, spectra were traced on the continuum lamp exposure obtained before each science exposure, and wavelength calibrated using a HgNe arc lamp. The continuum lamp and sky flats were used to determine the response of the instrument for each fiber and wavelength. Finally, for the standard stars we have co-added the spectra of the central fibers and compared them with the tabulated one-dimensional spectra.

We have noticed the effect of the differential atmospheric refraction (DAR) in the monochromatic images of HH 202 obtained for Balmer lines at different wavelengths reaching the value of $\sim1\farcs3$ between Hα and H11. We have measured offsets between all Balmer line images, and shifted with respect to Hα. The maximum coincident FOV resulting in the whole wavelength range is $15''\times15''$. All the maps involving emission line ratios analysed in this paper have been corrected for DAR.

Due to the relatively low spectral resolution of the observations, Hg 4358 Å telluric emission was somewhat blended with [O III] 4363 Å and a proper sky subtraction was necessary. We have taken a median value of the Hg 4358 Å line flux (9.22×10^{-16} erg cm^{-2} s^{-1}), which is in some regions approximately two orders of magnitude lower than the auroral line flux.

In previous works the background nebular emission in Orion proplyds has been determined, either using echelle data (Henney & O'Dell 1999) or integral field spectroscopy (Vasconcelos et al. 2005). In our case, the low spectral resolution of the data does not allow to separate the HH 202 emission from the background. Furthermore, as pointed out in both cited papers, this task is very challenging due to small-scale inhomogeneities in the nebular emission. As a result, only rough estimates can be given. Using the method proposed by Vasconcelos et al. (2005), we have assumed that the background emission is represented by the emission in the northeast corner of the FOV. The resulting background contribution is thus estimated to lie between 40% and 50% in knot HH 202-S, and between 55% and 65% in the rest of HH 202. If such a correction were applied to our data, we would obtain much larger densities, lower temperatures

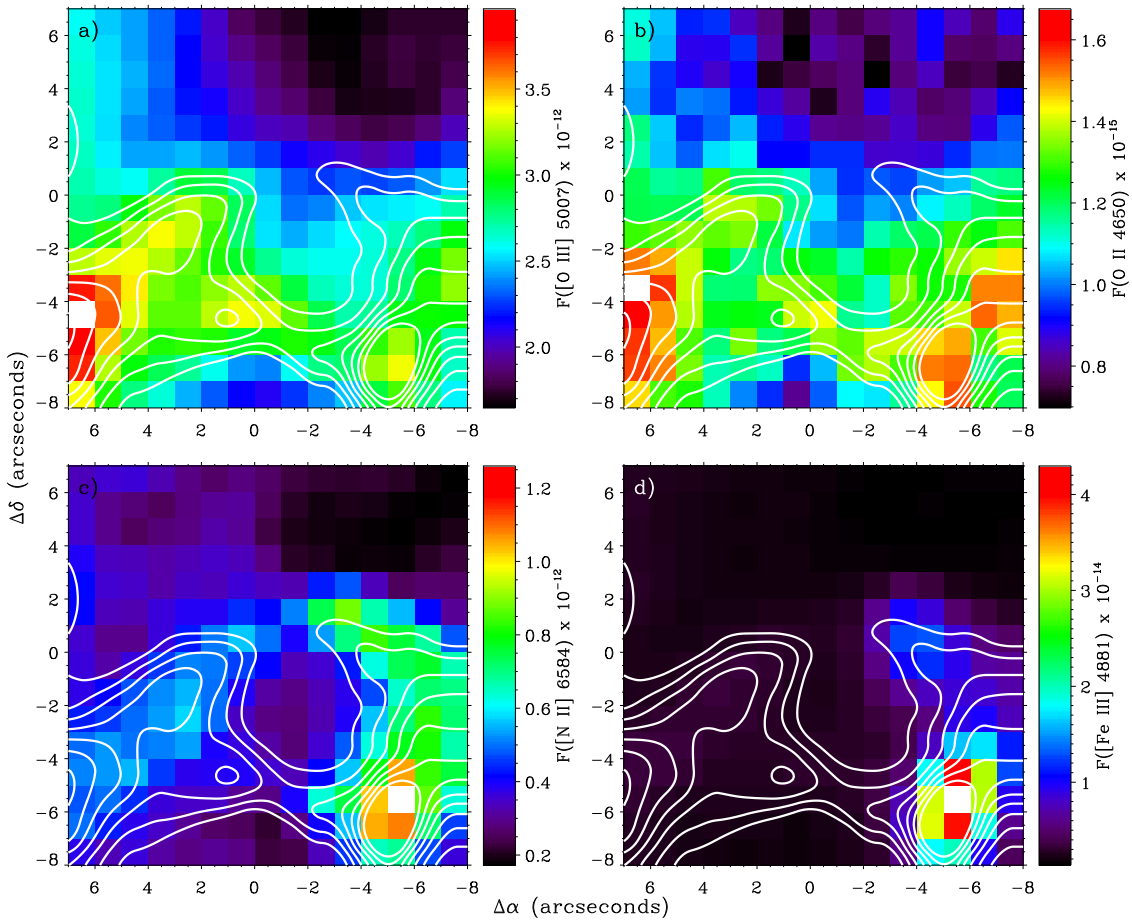

Figure 3. Emission line flux maps with Hα contours overplotted on the HH 202 PMAS field of: a) [O III] 5007 Å, b) O II 4650 Å, c) [N II] 6584 Å and d) [Fe III] 4881 Å (in units of erg cm^{-2} s^{-1}).

from the [N II] line ratio and higher temperatures from the [O III] line ratio with respect to the results presented in next sections. These results do not change the final conclusions of the paper because we are interested in how the presence of an HH object affects to the ADF when low spectral resolution observations are made and the contributions from the gas flows and the nebular background are mixed. In Paper II, we perform a complete analysis of the knot HH 202-S based on echelle spectrophotometry. The high resolution of these data has allowed us to resolve the kinematic component associated with the gas flow and the one associated with the background emission (in a small area included in the PMAS field). This analysis indicates that the background emission ranges from 30% in the case of [N II] 5755 Å to 60% for [O III] 5007 Å. In the case of H I lines, the background emission is about 50%.

3 LINE MEASUREMENTS AND REDDENING CORRECTION

The emission lines considered in our analysis are the following: a) Balmer lines, from Hα to H11, which are used to compute the reddening correction and correct the DAR shift (H8 and H10 were not used because they suffer from line-blending); b) CELs of various species, which are used to compute physical conditions and ionic abundances; c) Faint RLs of C II and O II which are used to derive the ionic abundances and to compute the ADF(O^{2+}). In Figure 2, we show an example of the spectra of a given spaxel where we can see the blend of O II lines at 4649 and 4651 Å.

Line fluxes were measured applying a single or a multiple Gaussian profile fit procedure between two given limits and over the local continuum. All these measurements were made with the SPLOT routine of IRAF and using our own scripts to automatize the process. The errors associated with the line flux measurements were determined following Mesa-Delgado et al. (2008). The final error of a line was computed as the quadratic sum of the error in its flux measurement and the error in flux calibration. In order to avoid spurious weak line measurements, we imposed three criteria to discriminate between real features and noise: 1) Line intensity peak over 2.5 times the sigma of the continuum; 2) FWHM(H I)/1.5 $<$ FWHM(λ) $<$ 1.5$\times$FWHM(H I); and 3) F(λ) $>$ 0.0001 $\times$ F(Hβ).

All line fluxes of a given spectrum have been normalized to Hβ and Hα for the blue and red range, respectively. To produce a final homogeneous set of line ratios, all of them were re-scaled to Hβ. The re-scaling factor used in the red spectra was the theoretical Hα/Hβ ratio for the physical conditions

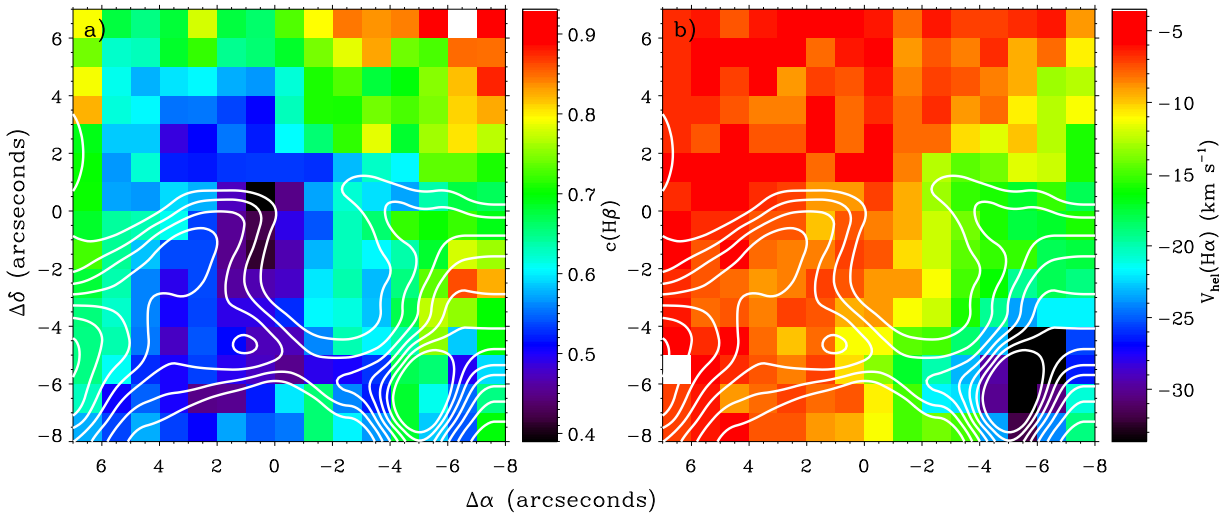

Figure 4. HH 202 PMAS maps with Hα contours overplotted. a) c(Hβ), b) Hα heliocentric velocity.

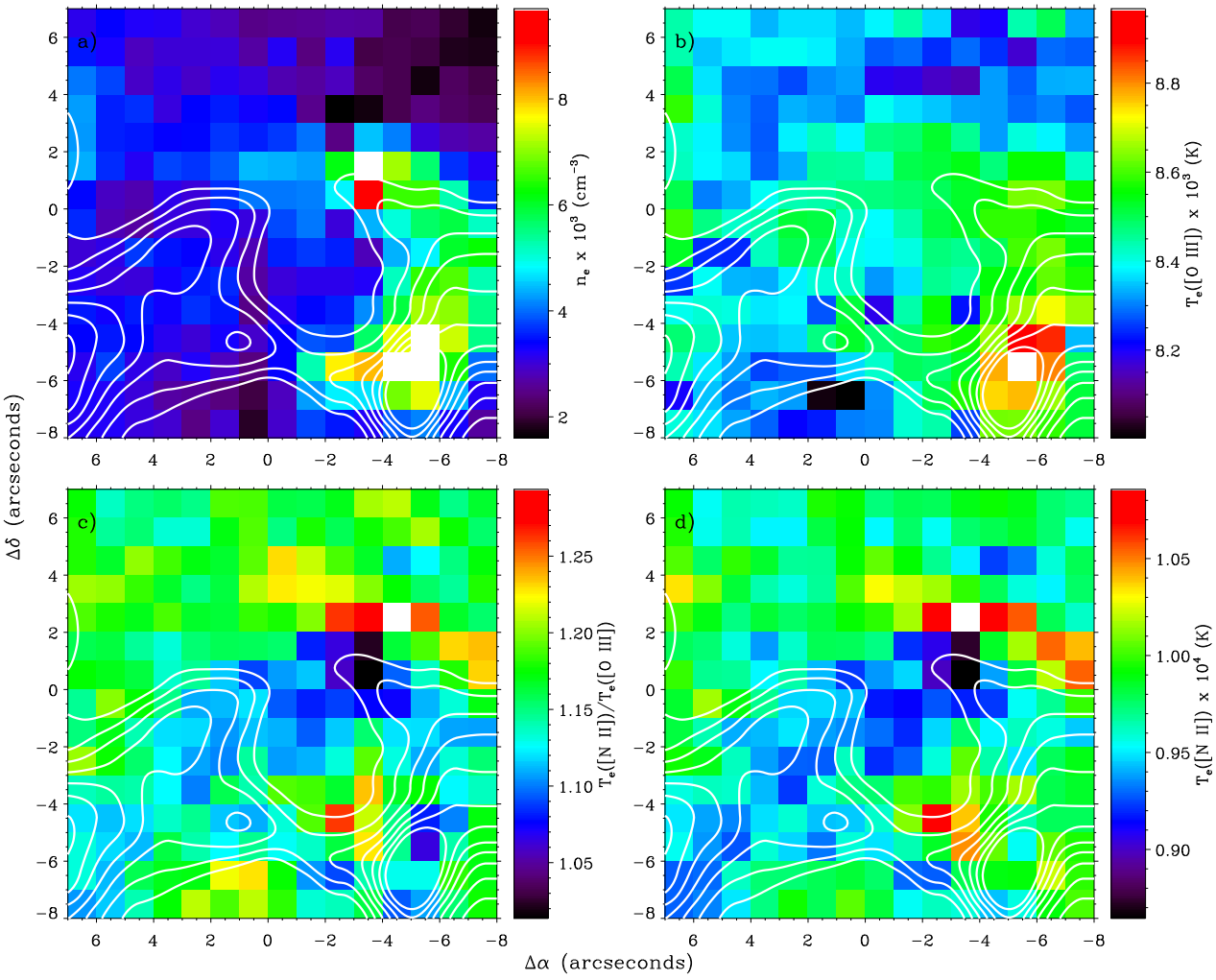

Figure 5. Physical conditions maps with Hα contours overplotted: a) n_e([S II]), b) T_e([O III]), c) T_e([N II])/T_e([O III]) ratio and d) T_e([N II]).

of T_e= 10000 K and n_e= 1000 cm^{-3}.

In Figure 3, we show [O III] 5007 Å, O II 4650 Å, [N II] 6584 Å and [Fe III] 4881 Å emission line maps with Hα contours overplotted. In Figures 3a and 3b, it is possible to see that the [O III] 5007 and O II 4650 Å spatial distributions are quite similar. In particular, the O II flux map seems to peak at the position of the apex of HH 202, the zone also known as HH 202-S –spaxels (-5.5,-6.5) and (-6.5,-4.5)–. A similar spatial distribution of both kinds of lines was already observed using long-slit spectra in the Orion Nebula by Mesa-Delgado et al. (2008), as well as in the three PNe observed by Tsamis et al. (2008b). Figure 3 also shows that the spatial distributions of [N II] and [O III] are rather different. The [N II] map shows an enhancement in the bow shock of HH 202. HH objects are characterized by their strong emission in [Fe III] lines. In Figure 3d we can see the spatial distribution of [Fe III] 4881 Å where the maximum emission is strongly concentrated at HH 202-S, which coincides with the maxima in radial velocity and electron density as we can see in Figures 4b and 5a. This high [Fe III] emission at HH 202-S may be related to shock destruction of dust grains or to the particular excitation conditions of the gas in the knot.

The reddening coefficient, c(Hβ), has been obtained by fitting the observed Hγ/Hβ, Hδ/Hβ, H9/Hβ and H11/Hβ ratios to the theoretical ones predicted by Storey & Hummer (1995) for n_e = 1000 cm^{-3} and T_e = 10000 K. We have used the reddening function, $f(\lambda)$, normalized to Hβ determined by Blagrave et al. (2007) for the Orion Nebula. The use of this extinction law instead of the classical one of Costero & Peimbert (1970) produces c(Hβ) values about 0.1 dex higher and dereddened fluxes with respect to Hβ about 3% lower for lines in the range 5000 to 7500 Å, 4% higher for wavelengths below than 5000 Å and 2% for wavelengths above 7500 Å. The final adopted c(Hβ) value for each spaxel is an average of the individual values derived from each Balmer line ratio weighted by their corresponding uncertainties. The typical error of c(Hβ) is about 0.14 dex for each spaxel. The resulting extinction map is shown in Figure 4a. The extinction coefficient varies approximately from 0.4 to 0.7 dex and reaches the highest values –between 0.8 and 0.9 dex– in a low surface brightness area at the north of HH 202. Excluding this zone –which shows the largest line intensity uncertainties– we obtain a mean value 0.56±0.14 dex.

We have compared our c(Hβ) values with those obtained by O'Dell & Yusef-Zadeh (2000) and Mesa-Delgado et al. (2008) for the area of HH 202. The first authors have obtained consistent c(Hβ) values from the Hα/Hβ line ratio using calibrated *HST* images and from radio to optical surface brightness ratio. HH 202 is located between the contour lines of 0.2 and 0.4 dex on the maps of O'Dell & Yusef-Zadeh (2000). On the other hand, Mesa-Delgado et al. (2008), from long-slit spectroscopy passing precisely through HH 202-S, derive a c(Hβ) value of about 0.4±0.1 dex. Therefore, we find that our mean value of the reddening coefficient is consistent with the previous determinations taking into account the errors and the different extinction laws used.

The heliocentric velocity map obtained from the centroid of the Hα line profile is shown in Figure 4b. We observe that the gas around the head of HH 202 shows a velocity of about −5 km s^{-1} and that the most negatives values are reached at HH 202-S position, where velocities of −35 km s^{-1} are measured. These values of the velocity of HH 202-S agree within the errors with that determined by Doi et al. (2004) of −39±2 km s^{-1} for this position. However, due to the lower spectral resolution of our data, the velocities we measure correspond to the blend of the emission of the background nebular gas and the gas flow of the HH object.

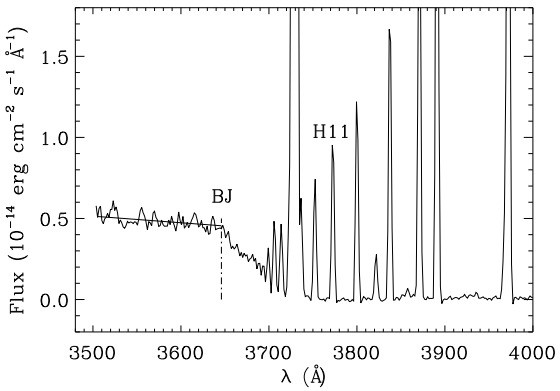

Figure 6. Section of a PMAS spectrum of the brightest spaxel at the apex (-5.5,-6.5). The fitted continuum contribution to the right side of the BJ was substracted to the whole range showed.

4 RESULTS

4.1 Physical conditions

Nebular electron densities, n_e, and temperatures, T_e, have been derived from the usual CEL ratios –[S II] 6717/6731 for n_e, and [O III] (4959+5007)/4363 and [N II] (6548+6584)/5755 for T_e, and using the TEMDEN task of the NEBULAR package of IRAF (Shaw & Dufour 1995) with updated atomic data (see García-Rojas et al. 2005). Following the same procedure as Mesa-Delgado et al. (2008) for the determination of the physical conditions, we have assumed an initial T_e= 10000 K to derive a first approximation of n_e, then we calculate T_e([O III]) and T_e([N II]), and iterate until convergence. We have not corrected the observed intensity of [N II] 5755 Å for contribution by recombination when determining T_e([N II]) because this contribution is expected to be rather small in H II regions with high ionization degree such as the Orion Nebula (e.g. Esteban et al. 2004). Bidimensional maps of n_e, T_e([O III]), T_e([N II])/T_e([O III]) ratio and T_e([N II]) are shown in Figures 5a, 5b, 5c, and 5d, respectively.

In Figure 5a we can see that the highest densities are just reached at the positions of HH 202-N and HH 202-S with values of about 10000 cm^{-3}. Similar values were obtained by Mesa-Delgado et al. (2008) for HH 202-S. For the gas outside the HH object, we find a n_e of about 4000 cm^{-3} and the lowest densities (∼2500 cm^{-3}) at the low surface brightness region at the northwest corner of the FOV. The typical errors in our density determination are between 200 and 250 cm^{-3}.

Figure 5b shows that T_e([O III]) is rather constant in the whole FOV. However, the highest values of T_e([O III]) trace the form of HH 202 –with an almost constant temperature

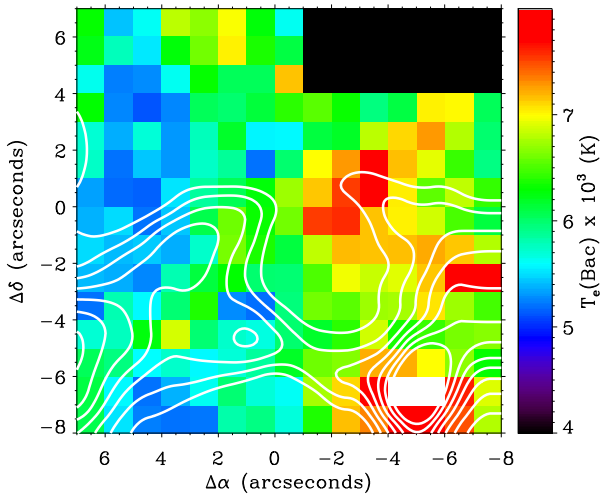

Figure 7. Balmer temperature map with Hα contours overplotted. The black rectangle on the northwest corner corresponds to an area masked due to the bad determination of T_e(Bac).

of 8500 K– reaching the peak value at the HH 202-S position where shock heating should be maximum. On the other hand, T_e([N II]) shows a much wider range of values across the FOV, but its spatial distribution is completely different to that of T_e([O III]). The maximum values of T_e([N II]) are found just behind HH 202-S or ahead of the northwest border of the bow shock of HH 202-N (see Figure 5d). The lowest values are found in the inner part of HH 202 (∼9500 K). In Figure 5c, the T_e([N II])/T_e([O III]) ratio illustrates that T_e([N II]) is always higher than T_e([O III]) but the ratio tends to be closer to one in the HH object and especially at HH 202-N where the density is higher. The uncertainties of the temperatures are about 600 K for T_e([N II]) and 250 K for T_e([O III]).

The Balmer continuum temperature, T_e(Bac), of the ionized gas has also been determined for most of the individual spaxels of the FOV; this is the first bidimensional T_e(Bac) map ever obtained for an ionized nebula. This temperature depends on the ratio between the Balmer jump (BJ) and the intensity of a given Balmer line. We have measured the BJ subtracting the continuum fitted at both sides of the Balmer discontinuity at 3646 Å (see Figure 6). The continuum fitted at both sides of the BJ is defined over spectral ranges free of emission lines covering the possible maximum baseline. The errors associated with the continuum subtraction are included in the discontinuity measurements. Finally, we have computed T_e(Bac) in K from the ratio of the BJ to the H11 flux using the relation proposed by Liu et al. (2001):

$$T_e(\mathrm{Bac}) = 368 \times \left(1 + 0.259y^{+} + 3.409y^{2+}\right)\left(\frac{\mathrm{BJ}}{\mathrm{H11}}\right)^{-\frac{3}{2}} \quad (1)$$

where y^+ and y^{++} correspond to the He^+/H^+ and He^{++}/H^+ ratios, respectively. We have assumed for y^+ the value derived by Esteban et al. (2004) for their slit position at the center of the Orion Nebula and $y^{++} = 0$ due to the lack of He II lines in our spectra. The effect of the interstellar extinction was taken into account in the calculations.

The T_e(Bac) map is shown in Figure 7. The T_e(Bac) error was calculated by error propagation in the equation (1), and it amounts to 22% on average (*i.e.*, 1100 to 1900 K). We can see that the lowest temperatures (∼5500 K) are reached at the east half of the FOV, while the west half shows values of about 7000 K, encompassing HH 202-S and HH 202-N. From the comparison of Figure 7 and the rest of the maps, we can see that the spatial distribution of T_e(Bac) is something similar that of T_e([O III]): both indicators show the maximum values at HH 202-S, HH 202-N and the arc connecting both features.

4.2 Chemical Abundances

The IRAF package NEBULAR has been used to derive ionic abundances of N^+, O^+ and O^{2+} from the intensity of CELs. We have assumed no temperature fluctuations in the ionized gas ($t^2 = 0$) and a two-zone scheme: T_e([N II]) for N^+ and O^+ –the low ionization potential ions– and T_e([O III]) for O^{2+}. The errors in the ionic abundances have been calculated as a quadratic sum of the independent contributions of errors in flux, n_e and T_e. The spatial distribution of the O^{2+} and O^+ abundances are presented in Figures 8b and 8d, respectively. In these figures, we can see that the spatial distributions of both abundances are completely different. The O^+/H^+ ratio reaches the highest values just on the bow shock, whereas O^{2+}/H^+ shows an inverse behaviour, reflecting the different ionization structure of the bow shock and the bulk of the background nebular gas. The higher O^+/O^{2+} ratio at the bow shock is probably produced by the higher densities in the shock gas, which increase the recombination rate of O^{2+}. The abundace map of N^+ –not presented here– shows a very similar distribution to the O^+ map.

The high signal-to-noise ratio of our spectra has permitted to detect and measure the weak RLs of O II and C II in all the spaxels of the PMAS FOV. These RLs have the advantage that their relative intensity with respect to a Balmer line is almost independent on T_e and n_e, largely unaffected by the possible presence of temperature fluctuations. In Figure 2 we show a section of the spectra at spaxel (-5.5, -6.5) around the O II lines.

We have measured the blend of the O II 4649 and 4651 Å lines –the brightest individual lines of the O II multiplet 1– in most of the spaxels of the FOV. In order to determine the O^{2+} abundance from this blend, we have combined equations (1) and (4) of Peimbert & Peimbert (2005) estimating the expected flux of all the lines of O II multiplet 1 flux with respect to Hβ, I(M1 O II)/I(Hβ). These relations were used in order to correct for the NLTE effects in the relative intensity of the individual lines of the multiplet, though these are rather small in the Orion Nebula due to its relatively large n_e. Then, the O^{2+}/H^+ ratio is calculated by:

$$\frac{\mathrm{O^{2+}}}{\mathrm{H^{+}}} = \frac{\lambda_{\mathrm{M1}}}{4861} \times \frac{\alpha_{eff}(H\beta)}{\alpha_{eff}(\mathrm{M1})} \times \frac{I(\mathrm{M1\ O\ II})}{I(H\beta)}, \quad (2)$$

where $\alpha_{eff}(H\beta)$ and α_{eff}(M1) are the effective recombination coefficients for Hβ and for the O II multiplet 1, respectively, and $\lambda_{\mathrm{M1}} = 4651.5$ Å the representative mean wavelength of the whole multiplet. We can also obtain the C^{2+} abundance using an equation analogous to (2) but using the specific quantities for this ion. Both abundances have been calculated assuming T_e([O III]) and with the effective recombination coefficients available in the literature (Storey 1994 for O^{2+} assuming LS coupling and Davey et al. 2000 for

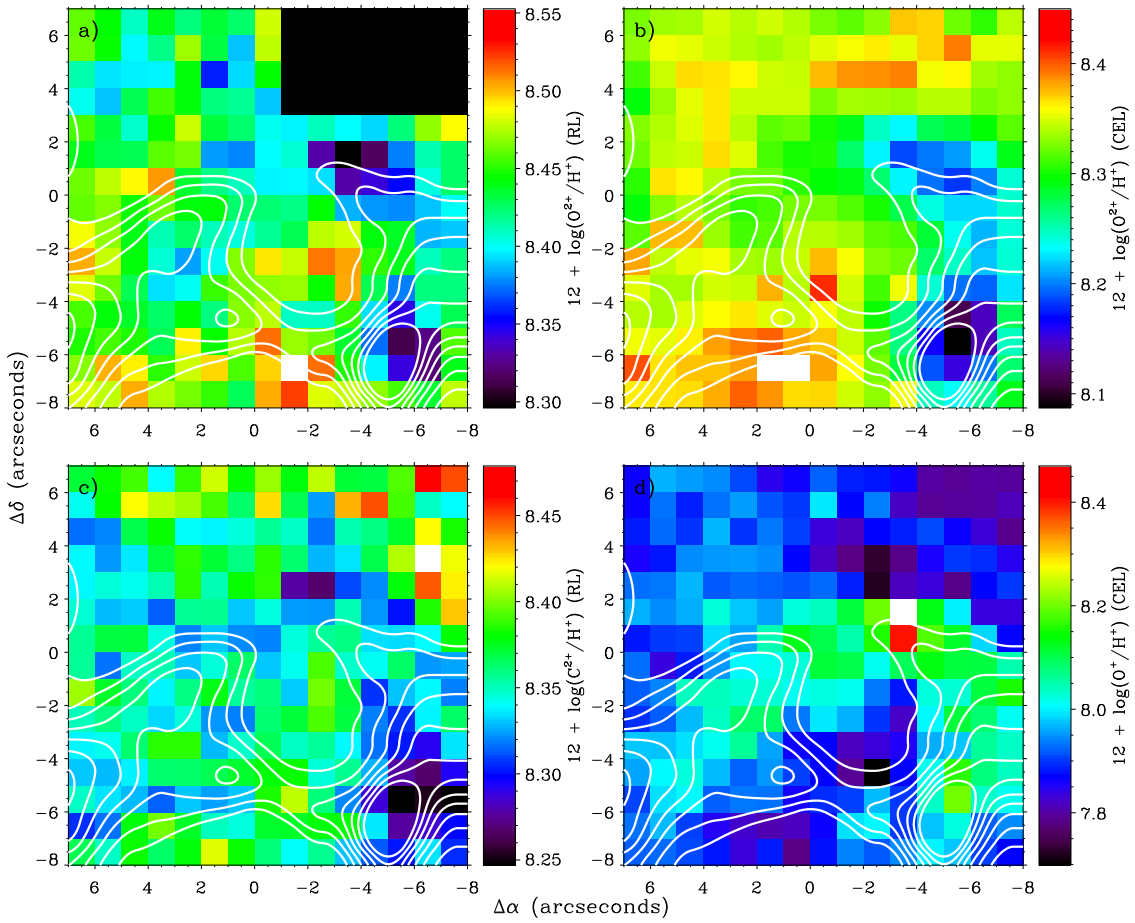

Figure 8. Ionic abundance maps with Hα contours overplotted: a) 12 + log(O^{++}/H^+) from RLs –the black rectangle on the northwest corner corresponds to an area masked due to the bad determination of the abundance, b) 12 + log(O^{++}/H^+) from CELs, c) 12 + log(C^{++}/H^+) from RLs and d) 12 + log(O^+/H^+) from CELs.

C^{2+}). Typical ionic abundance errors are 0.10 dex for O^{2+} and 0.08 dex for C^{2+}. The ionic abundances obtained from RLs are shown in Figures 8a and 8c.

The spatial distributions of the O^{2+} abundance obtained from CELs and RLs show that the lower values are found at the positions of HH 202-S and HH 202-N and the arc connecting both features. In contrast, the O^{2+} abundance map obtained from CELs shows especially large values in the zone inside the HH object at the bottom of the FOV. For a given spaxel, the O^{2+}/H^+ ratios obtained from RLs are always higher than those obtained from CELs, with a typical difference of about 0.10 dex. Finally, the C^{2+} abundance map shows rather constant values of about 8.35 dex, with its minimum value also found at HH 202-S. The qualitative behaviour of this map is rather similar to the O^{2+} abundance spatial distribution.

For each spaxel, the ADF(O^{2+}) has been calculated from the difference between the O^{2+} abundances obtained from RLs and CELs. In Figure 9, we show the spatial distribution of the ADF(O^{2+}), which shows the highest values at and around HH 202-S (up to 0.23 dex), the rest of the spaxels show values between 0.05 and 0.20 dex with a typical error value of 0.12 dex. Excluding the masked area showed in Figure 9, we have calculated an average value of 0.13 dex with

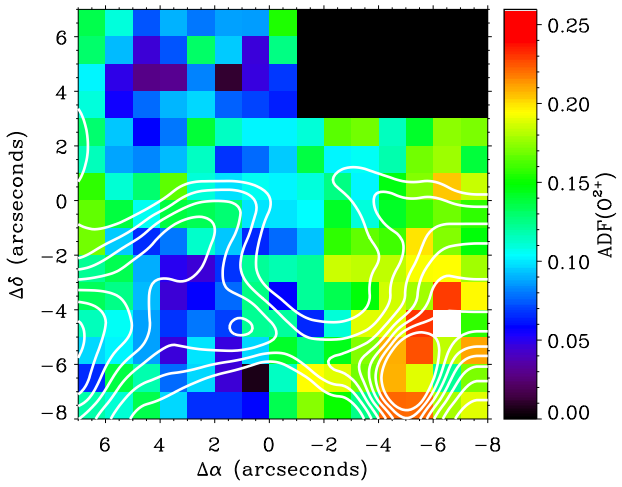

Figure 9. ADF(O^{2+}) map with Hα contours overplotted. The black rectangle on the northwest corner corresponds to an area masked due to the bad determination of the O^{2+} abundance from RLs.

a standard deviation of 0.05 dex. Mesa-Delgado et al. (2008) also found a peak of the ADF(O^{2+}) of about 0.30 dex at the same zone of HH 202. Both values of the discrepancy are consistent within the uncertainties, but the value obtained by those authors is, in principle, more reliable because of the better signal-to-noise ratio of their spectra.

5 DISCUSSION

5.1 Temperature fluctuations

One of the possible explanations for the AD problem in ionized nebulae is provided by the presence of temperature fluctuations (e.g. García-Rojas & Esteban 2007). Following Peimbert (1967), the temperature fluctuation over the observed volume of a nebula can be parameterized by

$$T_0 = \frac{\int T_e n_e n_i dV}{\int n_e n_i dV} \ , \qquad (3)$$

where T_0 is the average temperature of the nebula and n_i is the ion density, and

$$t^2 = \frac{\int (T_e - T_0)^2 n_e n_i dV}{T_0^2 \int n_e n_i dV} \ , \qquad (4)$$

where t^2 is the mean-square electron temperature fluctuation.

There are several methods to obtain t^2 and T_0 along the line of sight (see Peimbert et al. 2004). One possibility is to compare the T_e obtained from independent methods. Following Peimbert (1967), the temperature derived from the BJ depends on t^2 and T_0 as:

$$T_e(Bac) = T_0(1 - 1.70t^2) \ , \qquad (5)$$

and the temperatures derived from the ratio of CELs can be written as (Peimbert & Costero 1969)

$$T_e(\mathrm{h}) = T_0(\mathrm{h})\Big[1 + \frac{1}{2}\big(\frac{91300}{T_0(\mathrm{h})} - 3\big)t^2(\mathrm{h})\Big] \ , \qquad (6)$$

and

$$T_e(\mathrm{l}) = T_0(\mathrm{l})\Big[1 + \frac{1}{2}\big(\frac{69000}{T_0(\mathrm{l})} - 3\big)t^2(\mathrm{l})\Big] \ , \qquad (7)$$

where T_e(l) and T_e(h) are the electron temperatures for the low –T_e([N II])– and high –T_e([O III])– ionization zone, respectively. On one hand, we can obtain the $t^2(O^{2+})$ and $T_0(O^{2+})$ combining equations (5) and (6). On the other hand, $t^2(N^+)$ and $T_0(N^+)$ can be obtained combining expressions (5) and (7). To obtain the mean square temperature fluctuation for the entire volume, t^2, we have weigthed the relative importance of $t^2(N^+)$ and $t^2(O^{2+})$ in the observed volume by using equation 16 of Peimbert et al. (2002), assuming that in this region N^+ and O^+ coexist in the same volume. In Figures 10a, 10c and 10e, the $t^2(O^{2+})$, $t^2(N^+)$ and $< t^2 >$ maps are presented. Their associated error maps are also shown in Figures 10b, 10d and 10f.

The inspection of Figures 10b, 10c and 10e indicates that the spatial distribution of t^2 values are rather similar, showing somewhat lower t^2 values at the positions of HH 202-S and HH 202-N. We have calculated the mean value of $< t^2 >$ in the area where this quantity has been determined weighting the individual values of the fluctuation for each spaxel by its associated error, obtaining $< t^2 > \approx 0.061 \pm 0.022$.

Another possibility to obtain the t^2 parameter is assuming that the ADF(O^{2+}) is produced by the presence of temperature fluctuations. Following this assumption, we have used equations (9), (10) and (11) from Peimbert et al. (2004) to derive the associated $t^2(O^{2+})$ for each spaxel that –as expected– shows a spatial distribution analogous to the ADF map shown in Figure 9. In this case, the mean value of t^2 is only slightly lower than that obtained from the data of Figure 10a. A remarkable result is that the t^2 maps obtained from the two different methods –comparison of temperatures and from the ADF(O^{2+})– are qualitatively different suggesting, in this case, that there is not a genetic relationship between t^2 and ADF(O^{2+}).

Finally, we have determined the t^2 in the plane of the sky, t^2_A, using equations (11) and (12) of Mesa-Delgado et al. (2008), averaging the bidimensional point-to-point variations of $T_e(O^{2+})$ and $T_e(N^+)$. The values obtained are $t^2_A(O^{2+}) \sim 0.0004$ and $t^2_A(N^+) \sim 0.0023$, in agreement with the long-slit results by Mesa-Delgado et al. (2008), and substantially lower than the t^2 values obtained with the methods described in the previous paragraphs, which correspond to the fluctuations along the line of sight.

5.2 Correlations among the ADF and other nebular properties

In this section, we investigate some relationships among physical properties derived in the HH 202 PMAS field. In Figure 11 the possible correlations among the ADF(O^{2+}), T_e, n_e, c(Hβ), t^2 and ionic abundances determined from CELs and RLs are presented.

The dependence of the ADF(O^{2+}) with respect to c(Hβ), n_e, T_e([O III]), T_e(BJ), $t^2(O^{2+})$ and O^{2+}/O^+ ratio is shown from Figures 11a to 11f. Figure 11a –ADF(O^{2+}) *vs.* c(Hβ)– does not show a clear trend, indicating that the ADF does not depend on the amount of dust present in the line of sight of each spaxel of the PMAS field. As Mesa-Delgado et al. (2008) also obtained from their long-slit data, there seems to be no correlation between the ADF and n_e (see Figure 11b) as well as between the ADF and the ionization degree of the gas (see Figure 11f).

In Figures 11c and 11d, we can see that positive correlations are obtained between ADF(O^{2+}) *vs.* T_e([O III]) and ADF(O^{2+}) *vs.* T_e(BJ), respectively. This is expected because these three quantities show larger values at HH 202-S. As we can see in Figures 11c and 11d, these correlations do not seem very reliable considering the very narrow baseline of T_e([O III]) and T_e(BJ) covered by the data and the large error bars with respect to the baseline.

A rather unclear negative correlation between the ADF(O^{2+}) and the fluctuation parameter $t^2(O^{2+})$ along the line of sight can be guessed in Figure 11e. However, the large error bars in both quantities do not permit to establish any correlation. This result suggests the ADF and t^2 may be independent.

In Figures 11g, 11h and 11i, we represent the O^{2+} abundances from RLs, O^{2+} abundances from CELs and C^{2+} abundances from RLs *vs.* T_e([O III]), respectively. In the case of the abundances from RLs, we can observe negative correlations with rather low Spearman correlation coefficients ($\rho = -0.42$ and $\rho = -0.28$ for Figures 11g and 11i, respectively). This apparent trend is mainly produced by the be-

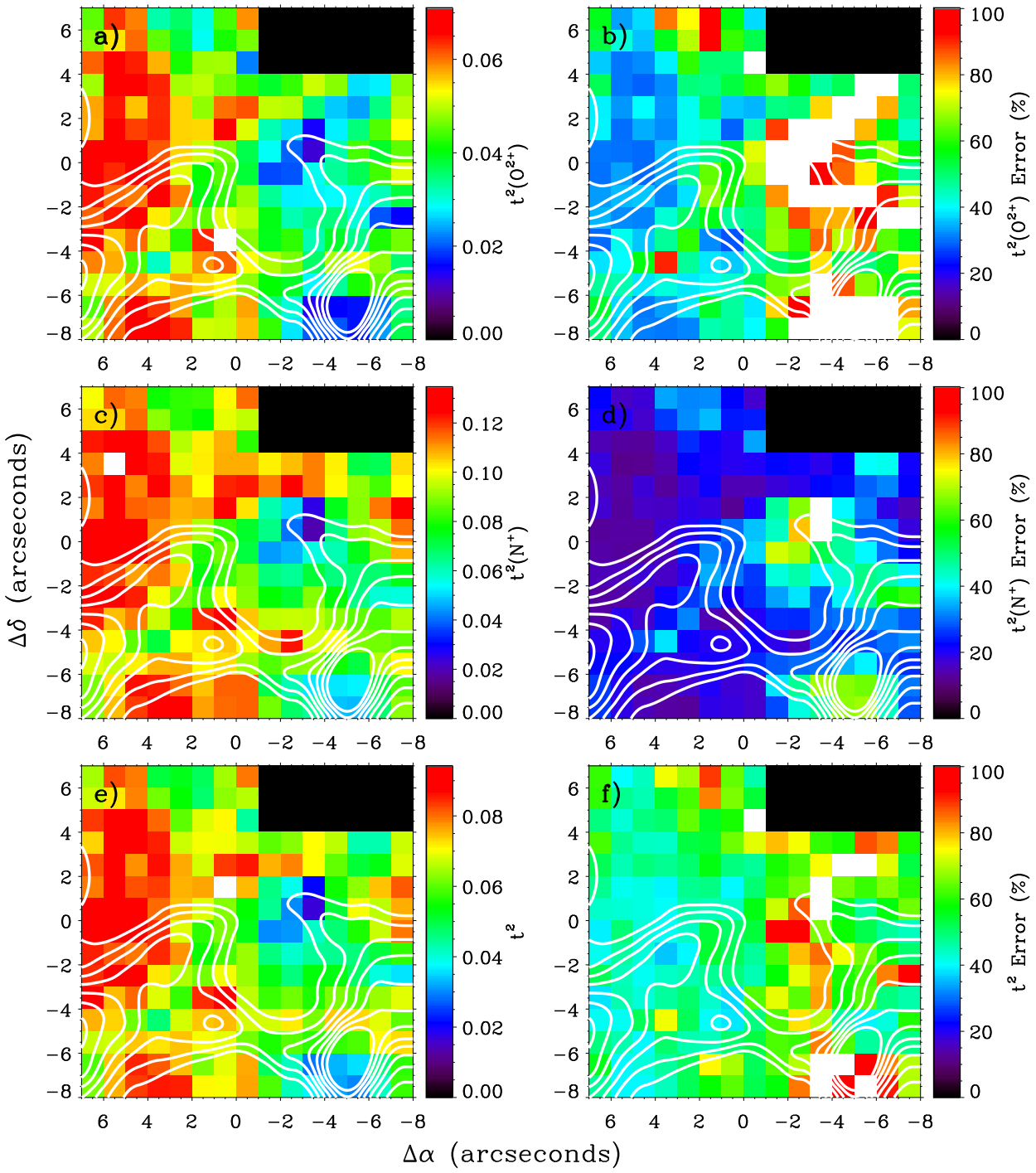

Figure 10. t^2 parameters and their respective error maps in percentage with Hα contours overplotted: a) and b) $t^2(O^{2+})$ and its error, c) and d) $t^2(N^+)$ and its error, e) and f) t^2 and its error. The white areas are where the error is higher than the t^2 value. The black rectangle on the northwest corner corresponds to an area masked due to the bad determination of T_e(Bac).

haviour observed at HH 202-S and HH 202-N, which are precisely the zones where the O^{2+} and C^{2+} abundances obtained from RLs are lower and T_e([O III]) is higher. From integral field spectroscopy, Tsamis et al. (2008b) have found rather clear positive correlations between ionic abundances obtained from RLs and T_e in three PNe, exactly the opposite trend we observe in this FOV of the Orion Nebula. These authors argue that their results provide evidence for the existence of two distinct components of highly ionized gas at very different temperatures. However, in this case, we observe the expected natural behaviour of an ionized nebula –the O^{2+} abundance from RLs increases when the temperature decreases– due to the fact that O^{2+} is a dominant coolant in the gas phase and the presence of spatial changes

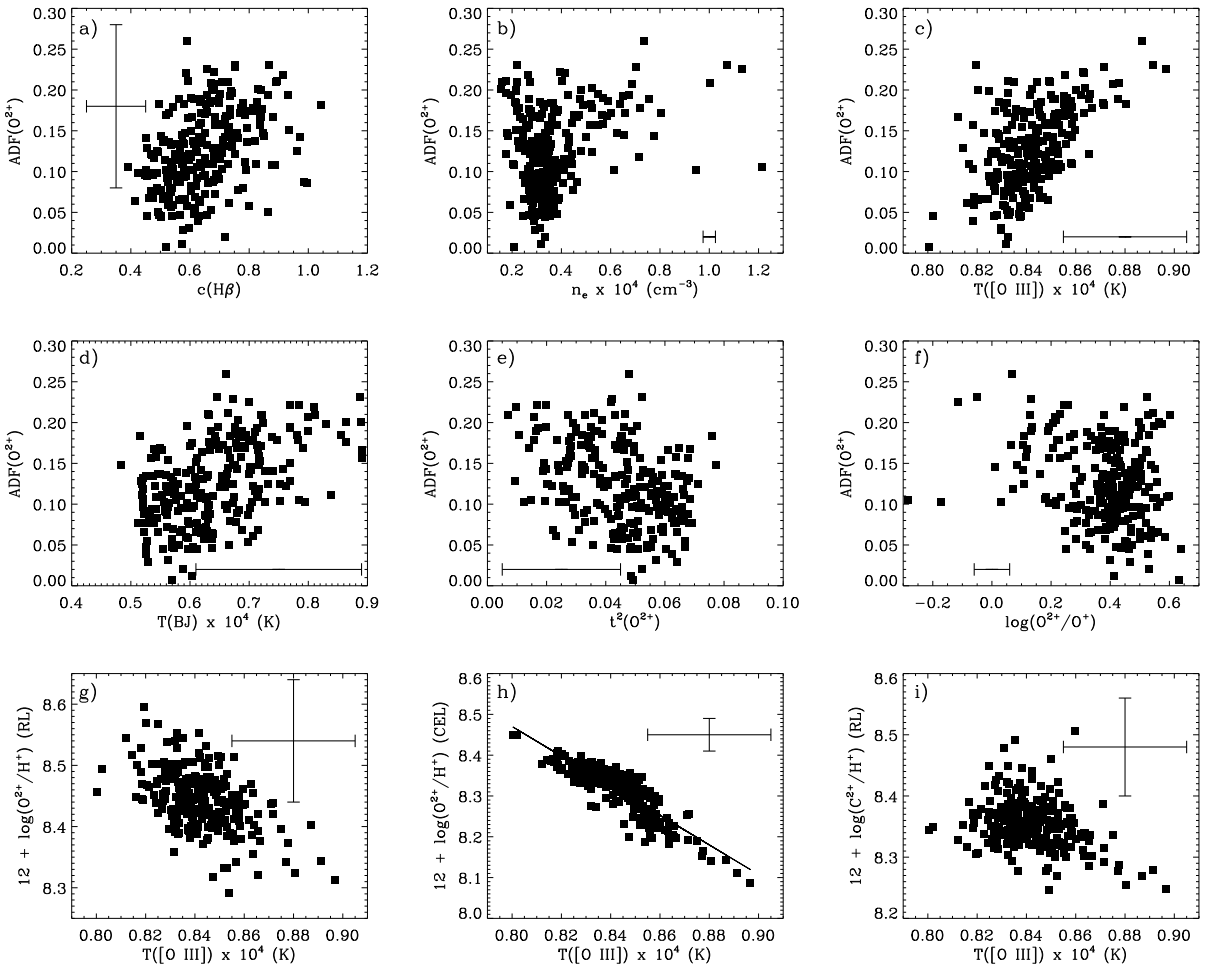

Figure 11. Correlations among different nebular properties obtained from PMAS maps. From a) to f) the ADF(O^{2+}) is represented with respect to c(Hβ), n_e, T_e([O III]), T_e(BJ), t^2[O III] and log(O^{2+}/O^+). The mean error bar in the ADF(O^{2+}) is only shown in a). From g) to i) the logarithmic abundances of O^{2+} from RLs, O^{2+} from CELs and C^{2+} from RLs are represented *vs.* T_e([O III]).

of the O^{2+}/O^+ ratio across the FOV. Therefore, the presence of metal-rich droplets does not seem to be supported by our results. On the other hand, the O^{2+}/H^+ ratio from CELs shows a much tighter correlation with T_e([O III]) due to the lower uncertainties of these abundances. We have fitted the following linear relation:

$$12 + \log(\frac{O^{2+}}{H^+}) = (11.4 \pm 0.1) + (-3.6 \pm 0.1)T_4 \qquad (8)$$

where T_4 is T_e([O III]) in units of 10^4 K and we have obtained a linear correlation coefficient $r = -0.90$.

6 CONCLUSIONS

In this paper, we present results from integral field spectroscopy of an area of $15'' \times 15''$ covering the head of HH 202 in the Orion Nebula. The FOV comprises the bright regions known as HH 202-S and HH 202-N. We have obtained maps of relevant emission line ratios, physical conditions and ionic abundances, including O^{2+} and C^{2+} abundances determined from recombination lines (RLs). Additionally, we have obtained maps of other interesting nebular properties, as the temperature fluctuation parameter, t^2, and the abundance discrepancy factor of O^{2+}, ADF(O^{2+}), which is defined as the difference between the O^{2+}/H^+ ratios determined from RLs and collisionally excited lines (CELs).

We find that the flux distributions of the [O III] and O II lines are rather similar and that the HH object is comparatively much brighter in the lines of low-ionization potential ionic species and especially in [Fe III]. The n_e is about 4000 cm^{-3} in most of the FOV and higher –about 10000 cm^{-3}– at HH 202-S and HH 202-N. The T_e([O III]) map shows a narrow range of variation, but the values are higher at HH 202-S. On the other hand, T_e([N II]) shows larger variations and a very different spatial distribution, being higher at the northern and eastern edges of HH 202-N and HH 202-S, respectively, a likely consequence of the ionization stratification or the presence of some shock excitation in the knots of the HH object. We have obtained –for the first time in an ionized nebula– the T_e(Bac) map, which follows closely that of T_e([O III]).

The O^+/H^+ ratio map reaches the highest values just on the arc that delineates the north of HH 202 from the east and west edges of the FOV, whereas the map of O^{2+} abundance

obtained from CELs shows an inverse behaviour, probably produced by the higher densities in the shock gas that increase the recombination rate of O^{2+}. The spatial distributions of the O^{2+} abundance obtained from CELs and RLs agree in showing the lower values at the positions of HH 202-S and HH 202-N and the arc connecting both features. However, for a given spaxel, the O^{2+}/H^+ ratios obtained from RLs are always about 0.10 dex higher than those obtained from CELs. The map of the ADF(O^{2+}) shows the highest values at and around HH 202-S.

We have determined –for the first time in an ionized nebula– the t^2 map of the FOV from the comparison of T_e(Bac) and the other T_e values determined from collisionally excited line ratios, finding that it does not match the ADF(O^{2+}) map. This result supports that the AD and temperature fluctuations are independent phenomena.

Finally, we have found weak correlations between the ADF(O^{2+}) and T_e values of the different spaxels of the FOV and between the O^{2+}/H^+ ratios obtained from RLs and CELs and T_e([O III]). The negative correlation between the O^{2+} abundances obtained from RLs and T_e([O III]) does not support the predictions of the chemical inhomogeneity models of Tsamis & Péquignot (2005) and Stasińska et al. (2007).

ACKNOWLEDGMENTS

We thank Sebastián F. Sánchez and the personnel of Calar Alto Observatory for their help with the observations. We are grateful to M. Peimbert, G. Stasińska and W. Henney for several suggestions and discussions. We also thank the referee of the paper for his/her positive comments. This work has been funded by the Spanish Ministerio de Ciencia y Tecnología(MCyT) under project AYA2004-07466 and Ministerio de Educación y Ciencia (MEC) under project AYA2007-63030 and 64712.

REFERENCES

Blagrave K. P. M., Martin P. G., Rubin R. H., Dufour R. J., Baldwin J. A., Hester J. J., Walter D. K., 2007, ApJ, 655, 299
Cantó J., Goudis C., Johnson P. G., Meaburn J., 1980, A&A, 85, 128
Costero R., Peimbert M., 1970, Boletin de los Observatorios Tonantzintla y Tacubaya, 5, 229
Davey A. R., Storey P. J., Kisielius R., 2000, A&AS, 142, 85
Doi T., O'Dell C. R., Hartigan P., 2002, AJ, 124, 445
Doi T., O'Dell C. R., Hartigan P., 2004, AJ, 127, 3456
Esteban C., Peimbert M., García-Rojas J., Ruiz M. T., Peimbert A., Rodríguez M., 2004, MNRAS, 355, 229
Esteban C., Peimbert M., Torres-Peimbert S., Escalante V., 1998, MNRAS, 295, 401
García-Rojas J., Esteban C., 2007, ApJ, 670, 457
García-Rojas J., Esteban C., Peimbert A., Peimbert M., Rodríguez M., Ruiz M. T., 2005, MNRAS, 362, 301
Henney W. J., O'Dell C. R., 1999, AJ, 118, 2350
Liu X.-W., Barlow M. J., Zhang Y., Bastin R. J., Storey P. J., 2006, MNRAS, 368, 1959
Liu X.-W., Luo S.-G., Barlow M. J., Danziger I. J., Storey P. J., 2001, MNRAS, 327, 141
Liu X.-W., Storey P. J., Barlow M. J., Danziger I. J., Cohen M., Bryce M., 2000, MNRAS, 312, 585
Meaburn J., 1986, A&A, 164, 358
Mesa-Delgado A., Esteban C., García-Rojas J., 2008, ApJ, 675, 389
O'Dell C. R., Doi T., 2003, AJ, 125, 277
O'Dell C. R., Hartigan P., Lane W. M., Wong S. K., Burton M. G., Raymond J., Axon D. J., 1997, AJ, 114, 730
O'Dell C. R., Henney W. J., 2008, Arxiv: 0807.4189
O'Dell C. R., Peimbert M., Peimbert A., 2003, AJ, 125, 2590
O'Dell C. R., Wen Z., Hester J. J., 1991, PASP, 103, 824
O'Dell C. R., Wong K., 1996, AJ, 111, 846
O'Dell C. R., Yusef-Zadeh F., 2000, AJ, 120, 382
Oke J. B., 1990, AJ, 99, 1621
Peimbert A., Peimbert M., 2005, in Torres-Peimbert D., MacAlpine G., eds, Rev. Mexicana Astron. Astrofis. Conf. Ser. Vol. 23, p. 9
Peimbert A., Peimbert M., Luridiana V., 2002, ApJ, 565, 668
Peimbert M., 1967, ApJ, 150, 825
Peimbert M., Costero R., 1969, Boletin de los Observatorios Tonantzintla y Tacubaya, 5, 3
Peimbert M., Peimbert A., Ruiz M. T., Esteban C., 2004, ApJS, 150, 431
Roth M. M., Kelz A., Fechner T., Hahn T., Bauer S.-M., Becker T., Böhm P., Christensen L., Dionies F., Paschke J., Popow E., Wolter D., Schmoll J., Laux U., Altmann W., 2005, PASP, 117, 620
Rubin R. H., Martin P. G., Dufour R. J., Ferland G. J., Blagrave K. P. M., Liu X.-W., Nguyen J. F., Baldwin J. A., 2003, MNRAS, 340, 362
Sánchez S. F., Cardiel N., Verheijen M. A. W., Martín-Gordón D., Vilchez J. M., Alves J., 2007, A&A, 465, 207
Shaw R. A., Dufour R. J., 1995, PASP, 107, 896
Stasińska G., Tenorio-Tagle G., Rodríguez M., Henney W. J., 2007, A&A, 471, 193
Storey P. J., 1994, A&A, 282, 999
Storey P. J., Hummer D. G., 1995, MNRAS, 272, 41
Tenorio-Tagle G., 1996, AJ, 111, 1641
Tsamis Y. G., Barlow M. J., Liu X.-W., Danziger I. J., Storey P. J., 2003, MNRAS, 345, 186
Tsamis Y. G., Barlow M. J., Liu X.-W., Storey P. J., Danziger I. J., 2004, MNRAS, 353, 953
Tsamis Y. G., Péquignot D., 2005, MNRAS, 364, 687
Tsamis Y. G., Walsh J. R., Péquignot D., 2008a, Arxiv: 0804.1100
Tsamis Y. G., Walsh J. R., Péquignot D., Barlow M. J., Danziger I. J., Liu X.-W., 2008b, MNRAS, 386, 22
Vasconcelos M. J., Cerqueira A. H., Plana H., Raga A. C., Morisset C., 2005, AJ, 130, 1707